Applied Surface Science 625 (2023) 157132

Contents lists available at ScienceDirect

Applied Surface Science

journal homepage: www.elsevier.com/locate/apsusc

Full Length Article

Surface properties, chemical reactivity, and ambient stability of cadmium diarsenide $CdAs_2$, a topological chiral material hosting Kramers-Weyl fermions

Yanxue Zhang [a,1], Gianluca D'Olimpio [b,*,1], Federica Bondino [c], Silvia Nappini [c], Marian Cosmin Istrate [d], Raman Sankar [e], Corneliu Ghica [d], Luca Ottaviano [b], Junfeng Gao [a,*], Antonio Politano [b,*]

[a] Key Laboratory of Materials Modification by Laser, Ion and Electron Beams (Dalian University of Technology), Ministry of Education, School of Physics, Dalian 116024, China
[b] Department of Physical and Chemical Sciences, University of L'Aquila, via Vetoio, 67100 L'Aquila (AQ), Italy
[c] Istituto Officina dei Materiali (IOM)–CNR, Area Science Park, S.S.14, km 163.5, I-34149 Trieste, Italy
[d] National Institute of Materials Physics, Atomistilor 405A, 077125 Magurele, Romania
[e] Institute of Physics, Academia Sinica Nankang, Taipei 11529, Taiwan

ARTICLE INFO

Keywords:
Surface chemical reactions
Ambient stability
Topological chiral material
Kramers-Weyl fermions
X-ray photoelectron spectroscopy

ABSTRACT

Chiral materials showing Kramers-Weyl fermions represent a suitable platform for quantum technology, i.e., for engineering quantum solenoids, spin-torque devices, polarization-sensitive photodetectors based on quantized circular photogalvanic effect, etc. Accordingly, the stability of this class of materials in oxidative environments, such as the ambient atmosphere, should be carefully investigated to succeed in technology transfer. Here, taking as case-study example the well-recognized topological chiral system cadmium diarsenide ($CdAs_2$), we assess its chemical reactivity towards ambient gases (oxygen and water) and air by density functional theory and experiments. The surface of $CdAs_2$ evolves into an oxide skin, but its thickness remains nanometric even after one year in air, as directly imaged by high-resolution transmission electron microscopy. Accordingly, it is evident that future quantum devices based on Kramers-Weyl fermions could be stable in air, as the oxide layer formed on chiral quantum materials only represents a native oxide, which actually protects bulk features, including Kramers-Weyl fermions (correlated to bulk band structure), from degradation in air.

1. Introduction

Quantum materials possessing topologically protected optical and electronic properties have paved the way for the development of opto-electronic devices that exploit the quantum properties of electrons in materials [1–8]. Recently, topological chiral crystals have gained significant attention [9–14]. These materials exhibit a lattice structure with a definite handedness due to missing inversion, mirror, and roto-inversion symmetries. In chiral crystals with spin–orbit coupling (SOC), each time-reversal invariant momentum (TRIM) becomes a Kramers-Weyl point [11,15]. Fermi surfaces enclosing Kramers-Weyl points are split by SOC, and each Fermi surface displays nontrivial and opposite Chern numbers. At the Kramers-Weyl points, the large Berry curvature implies a significant orbital contribution to the magnetization, leading to a negative longitudinal magnetoresistance.

Kramers-Weyl fermions in topological chiral crystal enable devising innovative spin–orbit torque devices with electric control of magnetization switching, as well as quantum solenoids[16]. Furthermore, the helicoidal Fermi surfaces of chiral crystals enable the emergence of the quantized circular photogalvanic effect [9], which is particularly relevant for engineering photodetectors with polarization dependence of photocurrent. This allows for the detection of both light intensity and polarization, in contrast to conventional photodetectors that exclusively detect light intensity [17].

It is essential for devices based on Kramers-Weyl fermions to operate in ambient atmosphere. Therefore, investigating the air stability of

* Corresponding authors.
E-mail addresses: gianluca.dolimpio@univaq.it (G. D'Olimpio), gaojf@dlut.edu.cn (J. Gao), antonio.politano@univaq.it (A. Politano).
[1] These authors contributed equally.

https://doi.org/10.1016/j.apsusc.2023.157132
Received 20 January 2023; Received in revised form 3 March 2023; Accepted 23 March 2023
Available online 25 March 2023

topological chiral materials is highly desirable to evaluate their evolution and ambient stability. Additionally, investigating the surface chemical reactivity towards water and oxygen could uncover potential applications of Kramers-Weyl crystals in catalysis. This is especially relevant given that most topological materials exhibit high values of electrical conductivity and charge-carrier mobility [18,19], facilitating rapid charge transfer in catalytic processes. Several studies have demonstrated the beneficial effects for kinetics resulting from the use of various classes of topological materials in catalysis [20–22].

As a model system, we chose cadmium diarsenide ($CdAs_2$), a topological chiral material [23] exhibiting negative magnetoresistance [24]. Here, we investigate surface properties and ambient stability of $CdAs_2$ topological chiral crystal using *ab initio* calculations and surface-science investigations.

We found that $CdAs_2$(1 1 0) has two equivalent surface terminations, both of which are metallic due to the emergence of surface states. Both surfaces are chemically unstable towards oxidation. The emergence of an oxide phase strongly affects the electronic properties of $CdAs_2$. However, the oxide skin remains nanometric even after one year in air, acting as a native oxide layer protecting the bulk from degradation in air. Moreover, $CdAs_2$ exhibits satisfactory stability in humid environments.

2. Methods

2.1. Theory

Our first-principles calculations were performed by using the Vienna ab-initio simulation package (VASP) [25]. Generalized gradient approximation (GGA) with the Perdew–Burke–Ernzerhof (PBE) functional [26] was used to describe the exchange–correlation interaction. The core electrons were descripted by the Projector-augmented wave (PAW) technology. A plane-wave basis kinetic energy cutoff of 500 eV and a convergence criterion of 10^{-5} eV were used in the calculations. All configurations were fully relaxed until the force is lower than 0.02 eV/Å. We adopted 0.02 1/Å k points sampling for structural relaxation. To explore the air stability of $CdAs_2$ surface, we calculated the kinetic barrier and path transition state for O_2 dissociation process on $CdAs_2$ surface by the climbing-image nudged elastic band method.

2.2. TEM

For the preparation of thin TEM samples, we applied either of two possible approaches in order to eliminate or reduce as much as possible the preparation artifacts related to the sample surface condition: i. reducing the samples to fine powder by crushing in a mortar or ii. mechanical polishing combined with ion milling using a Gatan PIPS installation. It is known that ion milling induces a certain surface damage of the crystalline samples which consists in a thin amorphous layer enveloping the ion milled sample. The thickness of this amorphous layer varies in function of the milling parameters such as accelerating voltage applied to the Ar ions, angle of incidence of the incident ion beams. In order to reduce this artifact and eliminate the amorphization layer, we finalized the ion milling step be reducing the accelerating voltage to 1 kV. However, whenever possible, we preferred to use the fine powder crushing as a “clean” method, devoid of any suspicion with respect to the processing-induced surface amorphization of the sample. The fine powder was dispersed in pure ethanol and a droplet from the liquid suspension was dripped onto a TEM grid provided with a lacey carbon membrane.

The samples were analyzed using a JEM ARM 200F transmission electron microscope provided with a Gatan Quantum SE spectrometer for analytical investigations by EELS. For the HRTEM investigation of the grains surface, we selected crystal grains hanging freely in the carbon membrane holes, with no membrane support underneath. The selected grains were tilted to the nearest available zone axis orientation, as shown in the SAED patterns. HRTEM micrographs were acquired from the thinnest regions at the grain border.

2.3. XPS

XPS measurements were carried out at the beamline BACH of IOM-CNR at the Elettra synchrotron radiation facility using a hemispherical electron analyzer (Scienta R3000) in a base pressure of 10^{-10} mbar. The spectra were acquired at normal incidence geometry and calibrated with Au-4f from a gold foil in electrical contact with the sample. Gases were dosed through leak valves in a high-pressure chamber with base pressure $< 5 \times 10^{-8}$ mbar connected to the measurement chamber. Water vapor was obtained through freeze–thaw cycles of milliQ liquid water and dosed through a leak valve. Purity of gas was checked by residual gas analyzer. Core-level spectra were fitted using Voigt line-shapes, after having subtracted a Shirley background.

3. Results and discussion

The optimized structure of $CdAs_2$ is a tetragonal lattice belonging to the space group no.98, $I4_122$, with a = b = 8.152 Å, c = 4.771 Å, according to our X-ray diffraction (XRD) results (Fig. S1 in Electronic Supplementary Information, SI). Cd and As atoms in the tetragonal lattice are arranged spirally (Fig. 1a). As atoms form spiral chains of covalent As–As bonds, whereas Cd–As bonds display a mixed ionic-covalent character (Fig. 1b). The natural cleavage plane is along the (1 1 0) direction. Therefore, we considered four possible surface terminations along the (1 1 0) direction: two surfaces terminated with As atoms (As1 and As2) and two with Cd atoms (Cd1 and Cd2), as shown in Fig. 1a. After relaxation of the surface structure, we obtained the optimized surface structure shown in Fig. 1c. The bond lengths of Cd-As bond in Cd1 surface increased mildly from 2.750 Å to 2.767 Å, while the bond lengths of As-As bond in As1 surface slightly decreased from 2.474 Å to 2.437 Å, indicating the considerable stability of As1 and Cd1 surfaces without any distortion. In contrast, the As2 and Cd2 surfaces underwent notable reconstruction. Specifically, the bond lengths of Cd-As bond in Cd2 surface decreased to 2.657 Å from the original value of 2.762 Å, and the bond angle of As-Cd-As increased from 133.707° to 159.564° after optimization. Moreover, the topmost Cd atoms in the Cd2 surface sank into the As-sublayer, which is similar to the self-passivation mechanism observed in the (1 1 2) surface of Cd_3As_2 topological Dirac semimetal [27]. The optimized As2 surface became chains with alternating lengths As-As, with the bond lengths of As-As bond decreased from 2.474/4.184 Å to 2.245/3.040 Å. Based on the optimized (1 × 1) surfaces, we also relaxed the (2 × 1) and (3 × 1) super-cells of As1, As2, Cd1, and Cd2 (Figure S4, SI), and found no further reconstruction. The bond lengths of As-Cd in Cd1 surface were close to the optimized (1 × 1) Cd1 surface, while the bond lengths of As-As bond in (2 × 1) and (3 × 1) As1 surface were similar to the optimized (1 × 1) surfaces. Similarly, the bond lengths of Cd-As bond in (2 × 1) and (3 × 1) Cd2 surface approached those of the optimized (1 × 1) Cd2 surface, and the bond lengths of As-As bond in (2 × 1) and (3 × 1) As2 surface were similar to those of the optimized (1 × 1) As2 surface. Thus, we focus on (1 × 1) surfaces as no new surface reconstruction was observed even under larger supercells.

In Fig. 1d, the surface formation energy of such four different surfaces as a function of the chemical potential of As atoms (μ_{As}) is shown. It is evident that the As1 surface termination has the lowest surface energy in the As-rich environments, while the Cd1 termination have the lowest surface energy in the As-poor environments. Besides, we also examined the surface energy as a function of μ_{As} for slab thickness ranging from 14 to 35 Å (Figure S2, SI), and found no influence on the surface atomic structure and the surface energy of the four surfaces (Figure S3, SI). Therefore, in the following, we focus our attention on the As1 and Cd1 surface terminations of $CdAs_2$(1 1 0).

We investigated two possible oxidation structures of As1 and Cd1

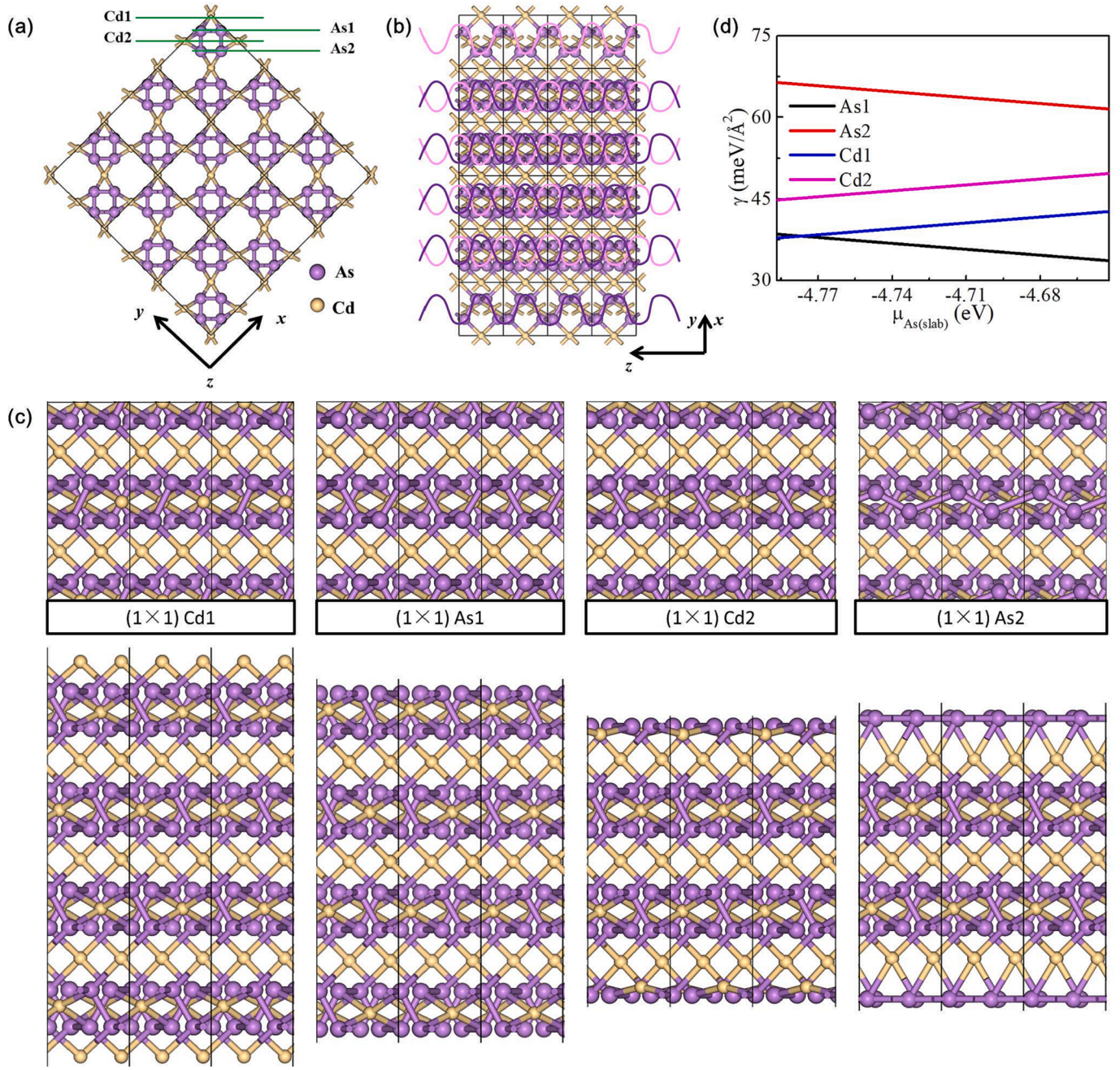

Fig. 1. (a) The top view of the optimized structure of bulk $CdAs_2$. Here, purple and yellow balls represent As and Cd atoms, respectively. The unit cell is marked by black solid lines. The four possible (1 1 0) surface terminations are highlighted by green lines. (b) The side view of (a). To guide the eye, pink and purple lines highlight the spiral structure. (c) The top (upper panel) and side (lower panel) views of the optimized surface with a thickness of 23 Å. The unit cell is marked by black solid lines. (d) The surface formation energy of different surfaces as a function of the chemical potential of As atoms (μ_{As}).

surfaces, as shown in Fig. 2a and 2b, respectively. The surface band structure of oxygenated As1- and Cd1-terminated $CdAs_2$ surfaces is shown in Fig. 2c and 2d, respectively. The oxygenated surface showed significant modifications to the band structure compared to the pristine $CdAs_2$ surface (see SI, Fig. S3 for the electronic structure of the pristine surface).

In the case of the As1 surface, the conduction and valence bands were shifted downwards, and the surface As atoms projection band marked by pink lines in Fig. 2c moved away from the Fermi energy level and became intrinsic bulk band. The surface states were mainly contributed by O atoms, as indicated by the red lines. On the other hand, the band dispersions of the Cd1 termination varied with thickness, as shown in Fig. S3e-h. The surface Cd atoms projection bands separated into two groups at the Y point under a thickness of 17 Å, while they exhibited four-fold degeneracy at the Y point under a thickness of 23 Å. When the thickness increased to 29 Å, the surface Cd atoms projection bands had the same dispersion as those at a thickness of 17 Å, and when the thickness further increased to 35 Å, the surface Cd atoms projected band dispersions were similar to those at a thickness of 23 Å.

We compared slab models of different thicknesses to understand the variation in band dispersion. When the thickness was equal to 17 Å and 29 Å, the up and bottom Cd atoms did not overlap, whereas they did overlap when the thickness was equal to 23 Å and 35 Å. Our results indicate that the arrangement of up and bottom surface Cd atoms did not significantly change the surface energy of the Cd1 surface but had a considerable influence on the surface Cd atoms' projection band

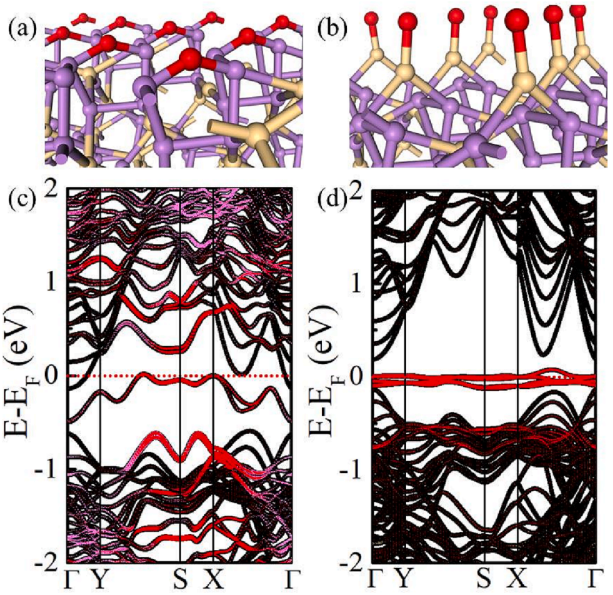

Fig. 2. The O-passivated structures for (a) As1-terminated and (b) Cd1-terminated (1 1 0) surfaces of $CdAs_2$, and their corresponding surface O (red lines), As (pink lines) and Cd (yellow lines) atoms projected band structures. Their corresponding electronic structure is reported in panels (c, d).

dispersions. Notably, the pristine Cd1 surface was always metallic, irrespective of whether the Cd atoms overlapped on the up and bottom surfaces.

In the oxidized Cd1 surface, the surface states of surface Cd atoms marked by yellow lines were effectively eliminated, and the surface states of surface O atoms mainly localized at the Fermi energy level.

Considering that technological applications based on $CdAs_2$ should work in air, we assessed the stability of the $CdAs_2$ surface in oxidative environments. To quantitatively assess the oxidation resistance of the $CdAs_2$ surface in an oxidative environment, we investigated the energetics of the oxidation process for the As1- and Cd1-terminated surfaces of $CdAs_2$. As shown in Fig. 3a, the initial state (IS) is the O_2 molecule chemically bonded to the As1 surface, and the final state (FS) is the O_2 molecule decomposed on the As1 (1 1 0) surface. To study the dissociation process of the O_2 molecule on the As1 (1 1 0) surface, we used the CI-NEB method with four inserted images. The O_2 molecule decomposed on the As1 surface releases energy of 3.79 eV compared to the initial chemical bonding, indicating that O_2 molecule dissociation on the As1 terminated (1 1 0) surface is energetically favourable. Specifically, O_2 molecule dissociation on the As1 surface has an energy barrier ΔE of only 0.22 eV (Fig. 3a), demonstrating that the As1 surface is prone to oxidation. The corresponding top and side views of the IS, transition state (TS), and FS are shown in Fig. 3a (bottom panel).

The oxidation rate of a surface can be described by the equation $R(T) = R\left(\frac{k_B T}{h}\right) \times exp(-\Delta E/k_B T)$, where T is the temperature, and k_B and h are the Boltzmann and Planck constants, respectively. At room temperature, the average oxidation rate for the As1 surface is approximately 10^9 s^{-1}, while for the Cd1 surface it is around 10^3 s^{-1}. This means that the As1 surface can be oxidized in a matter of nanoseconds in air, while it takes milliseconds for the Cd1 surface to undergo oxidation. However, at higher temperatures, the oxidation rate significantly decreases. For example, at 400 K, the average oxidation rate for the As1 surface is about 10^{10} s^{-1}, while for the Cd1 surface it is approximately 10^6 s^{-1}.

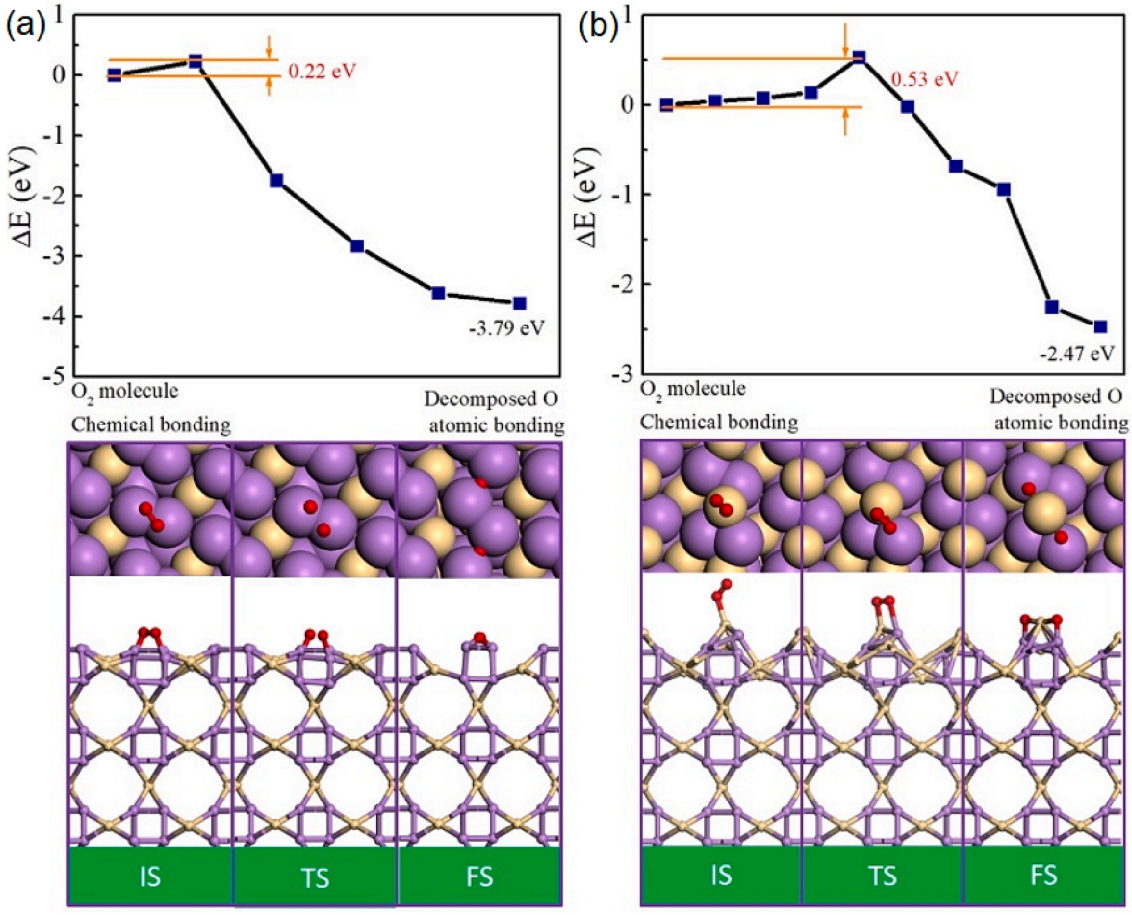

Fig. 3. Oxidation barriers ΔE and path of (a) As1-terminated and (b) Cd1-terminated (1 1 0) surfaces of $CdAs_2$.

The stability of $CdAs_2$ single crystals in oxidative and humid environments was investigated using surface-sensitive high-resolution X-ray photoelectron spectroscopy (XPS) experiments carried out with synchrotron radiation, which provided higher energy resolution and superior surface sensitivity. To obtain pristine surfaces, the (1 1 0)-oriented $CdAs_2$ single crystals were cleaved in ultra-high vacuum before being exposed to oxygen and water. The resulting data allowed for a detailed examination of the chemical states and changes in the surface composition of $CdAs_2$ under different environmental conditions.

Fig. 4 shows the evolution of (a) As-3d and (b) Cd-4d core levels in oxidative and humid environments. The as-cleaved $CdAs_2$ displays a single doublet peak in As $3d_{5/2}$ and Cd $4d_{5/2}$ at binding energy of 41.2 eV and 10.8 eV, respectively. After exposures to O_2 at room temperature, the only visible change is the progressive formation of elemental As(0) (As-As bond, associated with a As $3d_{5/2}$ component at 41.8 eV) [28] (Fig. 4a). Very weak (~9% of the total signal) components associated with the formation of Cd-O-As bonds and As_2O_3 appear only above $5x10^4$ L exposure [29]. The intensity of the main component in Cd core levels is progressively reduced, due to the presence of adsorbates and for the oxide layer. The component in O 1s at 530.3 eV (SI, Fig. S6) which appears after oxygen dosage is associated with both adsorbed oxygen atoms and oxidized species (As-O, Cd-O-As), formed due to the favorable O_2 molecule dissociation on the As atoms (see theoretical predictions in Fig. 3a). Thus, the exposure to oxygen-rich environment induces the selective oxidation of As atoms, with the formation of a thin As_2O_3 skin through intermediate steps, which include the formation of elemental As (0) and a few As-O-Cd intermediate oxides. Cd atoms are less affected by oxidation, as expected from the higher energy barrier found from theoretical calculations (Fig. 3b).

Upon exposure to H_2O, no significant chemical changes were observed with respect to the as-cleaved sample, except the formation of a small component due to As(0) (Fig. 4).

The inspection of the O-1s core level (SI, Fig. S7) indicates the progressive adsorption of OH and H_2O species. For a dosage of 4500 L, the presence of a component at 536 eV indicates that H_2O vapor is possibly trapped and stabilized under the first layer. Also, the Cd-4d and As-3d core levels remain unchanged, so one can conclude that no Cd-O or Cd-OH chemical bonds are formed. No As-O or Cd-O-As species are observed in either As-3d or Cd-4d. This finding indicates that $CdAs_2$ is relatively inert in a humid environment.

$CdAs_2$ crystals kept in air for one year display a high degree of oxidation with further species (Fig. 5, see also SI, Fig. S8 for O-1s), namely As_2O_5 [27,30], and Cd-OH, besides As(0), As-O-Cd and As_2O_3 [27], as in the case of direct exposure to O_2 [31].

To elucidate and quantify the robustness of topological chiral material in the ambient atmosphere, $CdAs_2$ was aged gradually, by exposing a freshly cleaved surface to air. After 10 min only Cd-O-As species are present, while after 3 h of air exposure spectral features related to hydroxilated Cd-OH, As_2O_3, and As_2O_5 emerge in both in Cd and As core levels. On the other hand, the sample kept in air for 1 year has intense oxide features.

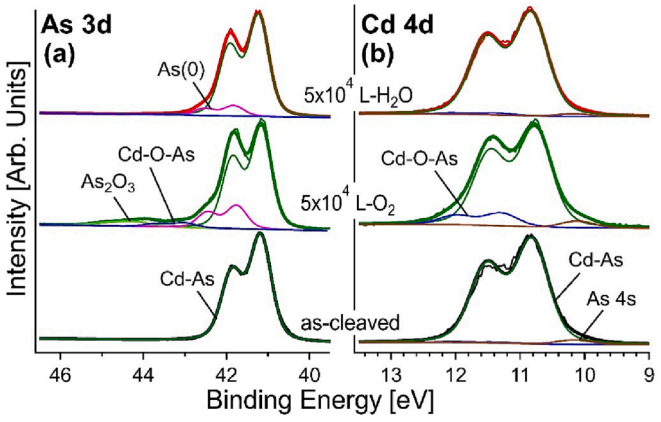

Fig. 4. Evolution of As-3d and Cd-4d core levels of as-cleaved $CdAs_2$ after O_2 and H_2O dosage.

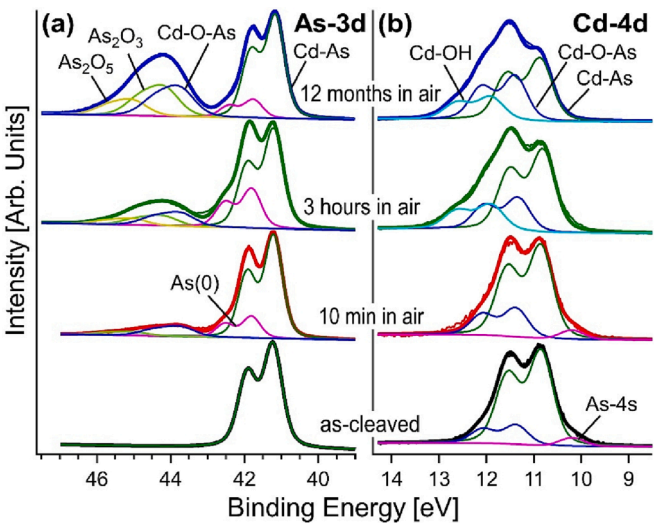

Fig. 5. Core-level spectra for $CdAs_2$ aged in air for a period extended up to one year. The photon energy was 608.5 eV.

To evaluate the thickness of the oxide layer, we conducted transmission electron microscopy (TEM) experiments. Additionally, we analyzed a typical $CdAs_2$ grain (Fig. 6a) using TEM and obtained the associated small-area electron diffraction (SAED) pattern (Fig. 6b) by tilting the grain to the nearest available zone axis orientation. Specifically, the zone axis orientation refers to the orientation of the crystal axis parallel to each crystal face in the crystal zone and through the origin of the coordinates. The SAED pattern was indexed according to the B = [1–1–1] zone axis orientation of the tetragonal structure of $CdAs_2$, with the unit cell parameters resulting from our XRD data in Fig. S1 of the SI. HR-TEM images were recorded from the thinnest regions at the grain border (pointed by arrows in Fig. 6a). At higher magnifications (Fig. 6c), one can notice the presence of an amorphous surface oxide layer with a rather uniform thickness of around 1.5 nm entirely enveloping the analyzed grain. A detail of the subsurface structure of the grain is shown in the HR-TEM micrograph in Fig. 6d. The (1 1 0) and (0–11) crystal planes separated at 0.56 nm and 0.4 nm, respectively, are indicated on the micrograph. The grain border runs almost parallel to the mentioned crystal planes.

4. Conclusions

In summary, this study has investigated the stability and surface properties of $CdAs_2$, revealing two stable (1 1 0) surfaces by considering four possible surface termination structures. Both As1 and Cd1 surfaces have been found to possess metallic character, owing to the existence of unsaturated surface states. Moreover, the As1 and Cd1 surfaces are rapidly oxidized in air, with relatively low energy barriers for spontaneous oxidation. The surface of $CdAs_2$ assumes an oxide skin when exposed to oxidative environments (including air), but its thickness remains at approximately 1.5 nm even after one year of exposure. Furthermore, this study has demonstrated that $CdAs_2$ is highly stable in humid environments.

Considering the potential applications of topological chiral materials with Kramers-Weyl fermions in the development of quantum solenoids, spin-torque devices, and polarization-sensitive photodetectors, our findings suggest that the efficiency of such quantum devices is unlikely to be degraded upon air exposure. The amorphous oxide skin (composed of both As_2O_3 and As_2O_5 phases) naturally encapsulates the underlying

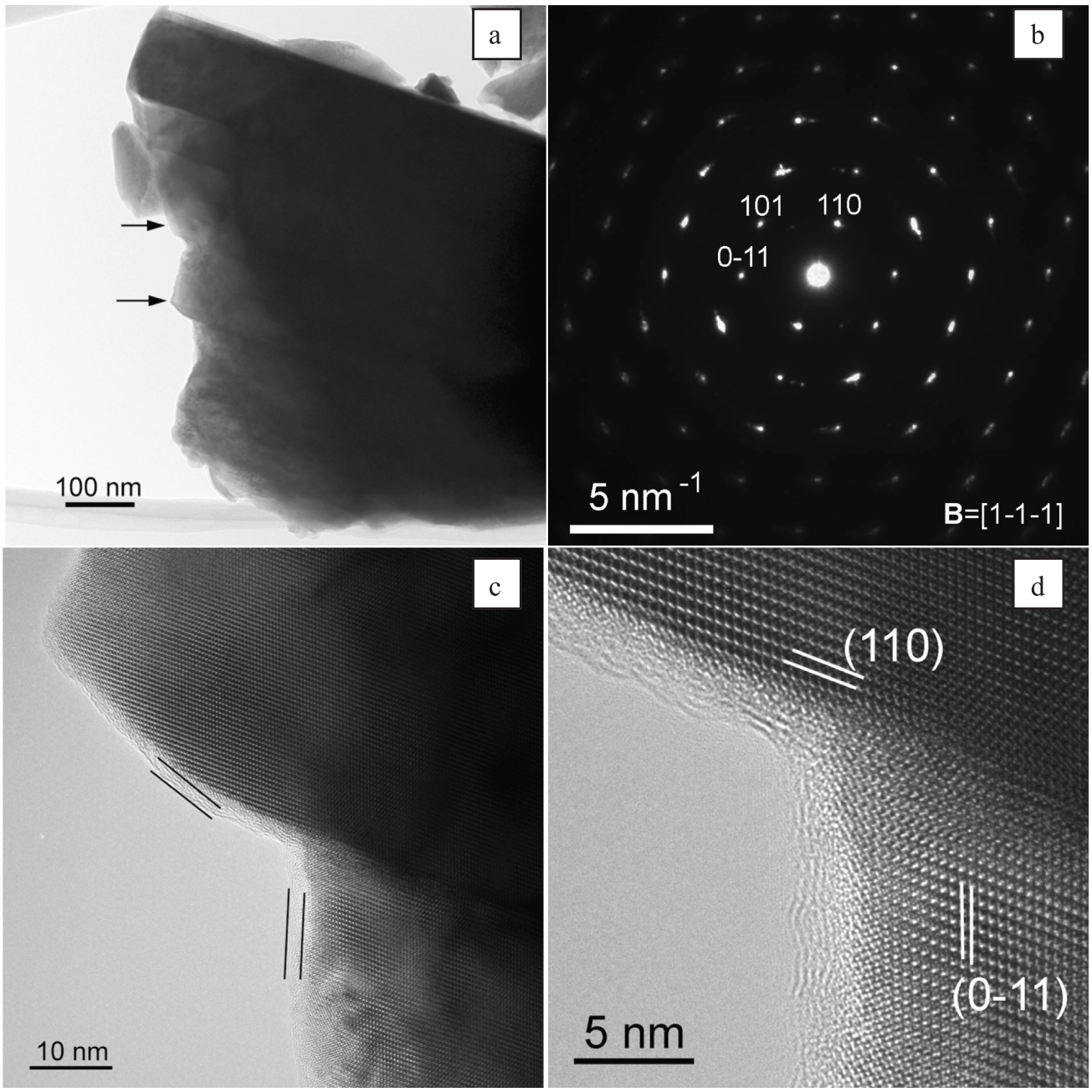

Fig. 6. (a) TEM image of a typical crystal grain from the $CdAs_2$ sample and (b) the associated SAED pattern along the B = [1–1–1] zone axis; (c) amorphous layer evidenced at the grain border; (d) HRTEM image showing the grain faceting parallel to the (1 1 0) and (0–11) crystalline planes of the tetragonal $CdAs_2$.

substrate, thereby protecting the bulk features of topological chiral materials, including Kramers-Weyl fermions.

Overall, this study provides valuable insights into the stability and surface properties of $CdAs_2$, highlighting the potential of topological chiral materials for future technological advancements in quantum computing and information processing.

CRediT authorship contribution statement

Yanxue Zhang: Formal analysis, Writing – original draft. **Gianluca D'Olimpio:** Conceptualization, Investigation, Data curation, Writing – original draft, Writing – review & editing. **Federica Bondino:** Investigation, Data curation, Writing – original draft. **Silvia Nappini:** Writing – original draft. **Marian Cosmin Istrate:** Investigation, Data curation. **Raman Sankar:** Investigation, Data curation. **Corneliu Ghica:** Investigation, Data curation. **Luca Ottaviano:** Investigation, Data curation. **Junfeng Gao:** Formal analysis, Writing – review & editing. **Antonio Politano:** Conceptualization, Writing – review & editing.

Declaration of Competing Interest

The authors declare that they have no known competing financial interests or personal relationships that could have appeared to influence the work reported in this paper.

Data availability

Data will be made available on request.

Acknowledgement

This work was supported by the National Natural Science Foundation of China (Grant No. 12074053, 91961204, 12004064), and National Foreign Expert Project (G2022127004L). C.G. and M.C.I. acknowledge funding through contract POC 332/390008/29.12.2020-SMIS 109522. R.S. acknowledges the financial support provided by the Ministry of Science and Technology in Taiwan under project numbers NSC-111-2124-M-001-009; NSC-110-2112-M-001-065-MY3; AS-iMATE-111-12.

Appendix A. Supplementary data

Supplementary data to this article can be found online at https://doi.org/10.1016/j.apsusc.2023.157132.

References

[1] H. Choi, J. Park, J.W. Shim, C. Shin, Negative quantum capacitance effect from $Bi_2Te_{1.5}Se_{1.5}$ with frequency dependent capacitance of polyvinyl alcohol (PVA) film in MOS structure, Appl. Surf. Sci. 463 (2019) 1046–1050.
[2] H. Choi, T.G. Kim, C. Shin, Measurement of the quantum capacitance from two-dimensional surface state of a topological insulator at room temperature, Appl. Surf. Sci. 407 (2017) 16–20.
[3] W. Yi, X. Jiang, Z. Wang, T. Yang, B. Yang, X. Liu, ABX_6 Monolayers: A new Dirac material family containing high Fermi velocities and topological properties, Appl. Surf. Sci. 570 (2021) 151237.
[4] G.K. Maurya, V. Gautam, F. Ahmad, R. Singh, K. Kandpal, R. Kumar, M. Kumar, P. Kumar, A. Tiwari, Visible to near-infrared broadband photodetector employing thin film topological insulator heterojunction (p-$TlBiSe_2$/n-Si) diode, Appl. Surf. Sci. 612 (2023), 155813.
[5] B. Ostahie, A. Aldea, Interface effects on the energy spectrum and quantum transport in two-dimensional topological heterostructures, Appl. Surf. Sci. 587 (2022), 152769.
[6] B. Turowski, A. Kazakov, R. Rudniewski, T. Sobol, E. Partyka-Jankowska, T. Wojciechowski, M. Aleszkiewicz, W. Zaleszczyk, M. Szczepanik, T. Wojtowicz, V.V. Volobuev, Spin-polarization of topological crystalline and normal insulator $Pb_{1-x}Sn_xSe$ (111) epilayers probed by photoelectron spectroscopy, Appl. Surf. Sci. 610 (2023), 155434.
[7] Y. Zhang, Y. Luo, C. Zhao, W. Chen, L. Liu, L. Zhang, Y. Jia, Z. Hou, First-principles study on the electronic structures and topological properties of Bi(110)/IV-VI and Bi(110)/V-V van der Waals heterostructures, Appl. Surf. Sci. 614 (2023), 156027.
[8] T. Yang, X. Jiang, W. Yi, X. Cheng, X. Liu, A g-SiC_6 monolayer and its analogs: A new class of tunable Dirac cone materials and novel quantum spin Hall insulators, Appl. Surf. Sci. 578 (2022), 151986.
[9] D.S. Sanchez, I. Belopolski, T.A. Cochran, X. Xu, J.X. Yin, G. Chang, W. Xie, K. Manna, V. Süß, C.Y. Huang, N. Alidoust, D. Multer, S.S. Zhang, N. Shumiya, X. Wang, G.Q. Wang, T.R. Chang, C. Felser, S.Y. Xu, S. Jia, H. Lin, M.Z. Hasan, Topological chiral crystals with helicoid-arc quantum states, Nature 567 (2019) 500–505.
[10] Y. Liu, X. Chen, Y. Xu, Topological phononics: from fundamental models to real materials, Adv. Funct. Mater. 30 (2020) 1904784.
[11] G. Chang, B.J. Wieder, F. Schindler, D.S. Sanchez, I. Belopolski, S.M. Huang, B. Singh, D. Wu, T.R. Chang, T. Neupert, S.Y. Xu, H. Lin, M.Z. Hasan, Topological quantum properties of chiral crystals, Nat. Mater. 17 (2018) 978–985.
[12] A. Inui, R. Aoki, Y. Nishiue, K. Shiota, Y. Kousaka, H. Shishido, D. Hirobe, M. Suda, J.I. Ohe, J.I. Kishine, H.M. Yamamoto, Y. Togawa, Chirality-Induced Spin-Polarized State of a Chiral Crystal $CrNb_3S_6$, Phys. Rev. Lett. 124 (2020), 166602.
[13] H. Li, S. Xu, Z.C. Rao, L.Q. Zhou, Z.J. Wang, S.M. Zhou, S.J. Tian, S.Y. Gao, J.J. Li, Y.B. Huang, H.C. Lei, H.M. Weng, Y.J. Sun, T.L. Xia, T. Qian, H. Ding, Chiral fermion reversal in chiral crystals, Nat. Commun. 10 (2019) 5505.
[14] M. Sakano, M. Hirayama, T. Takahashi, S. Akebi, M. Nakayama, K. Kuroda, K. Taguchi, T. Yoshikawa, K. Miyamoto, T. Okuda, K. Ono, H. Kumigashira, T. Ideue, Y. Iwasa, N. Mitsuishi, K. Ishizaka, S. Shin, T. Miyake, S. Murakami, T. Sasagawa, T. Kondo, Radial Spin Texture in Elemental Tellurium with Chiral Crystal Structure, Phys. Rev. Lett. 124 (2020), 136404.
[15] G. Chang, S.-Y. Xu, B.J. Wieder, D.S. Sanchez, S.-M. Huang, I. Belopolski, T.-R. Chang, S. Zhang, A. Bansil, H. Lin, Unconventional chiral fermions and large topological Fermi arcs in RhSi, Phys. Rev. Lett. 119 (2017), 206401.
[16] W.-Y. He, X.Y. Xu, K.T. Law, Kramers Weyl semimetals as quantum solenoids and their applications in spin-orbit torque devices, Commun. Phys. 4 (2021) 1–8.
[17] J.D. Yao, J.M. Shao, S.W. Li, D.H. Bao, G.W. Yang, Polarization dependent photocurrent in the Bi_2Te_3 topological insulator film for multifunctional photodetection, Sci. Rep. 5 (2015) 14184.
[18] J. Hu, S.-Y. Xu, N. Ni, Z. Mao, Transport of topological semimetals, Annu. Rev. Mater. Res. 49 (2019) 207–252.
[19] D. Culcer, A.C. Keser, Y. Li, G. Tkachov, Transport in two-dimensional topological materials: recent developments in experiment and theory, 2D, Mater. 7 (2020), 022007.
[20] A. Politano, G. Chiarello, Z. Li, V. Fabio, L. Wang, L. Guo, X. Chen, D. W. Boukhvalov, Toward the effective exploitation of topological phases of matter in catalysis: chemical reactions at the surfaces of NbAs and TaAs Weyl semimetals, Adv. Funct. Mater. 28 (2018) 1800511.
[21] Q. Qu, B. Liu, J. Liang, H. Li, J. Wang, D. Pan, I.K. Sou, Expediting Hydrogen Evolution through Topological Surface States on Bi_2Te_3, ACS Catal. 10 (2020) 2656–2666.
[22] Q. Yang, G. Li, K. Manna, F. Fan, C. Felser, Y. Sun, Topological Engineering of Pt-Group-Metal-Based Chiral Crystals toward High-Efficiency Hydrogen Evolution Catalysts, Adv. Mater. 32 (2020) 1908518.
[23] L. Červinka, A. Hrubý, The crystal structure of $CdAs_2$, Acta Crystallogr. B 26 (1970) 457–458.
[24] E. Żdanowicz, W. Wojciechowski, J. Misiewicz, K.G. Lisunov, Negative magnetoresistance for different orientations of n-type $CdAs_2$ in the variable-range hopping regime, Mater. Sci. Eng. B 26 (1994) 19–24.
[25] J. Hafner, Ab-initio simulations of materials using VASP: Density-functional theory and beyond, J. Comput. Chem. 29 (2008) 2044–2078.
[26] J.P. Perdew, K. Burke, M. Ernzerhof, Generalized Gradient Approximation Made Simple, Phys. Rev. Lett. 77 (1996) 3865–3868.
[27] J. Gao, A. Cupolillo, S. Nappini, F. Bondino, R. Edla, V. Fabio, R. Sankar, Y. W. Zhang, G. Chiarello, A. Politano, Surface Reconstruction, Oxidation Mechanism, and Stability of Cd_3As_2, Adv. Funct. Mater. 29 (2019) 1900965.
[28] C.J. Powell, Recommended Auger parameters for 42 elemental solids, J. Electron Spectrosc. Relat. Phenom. 185 (2012) 1–3.
[29] P. King, T.D. Veal, A. Schleife, J. Zúñiga-Pérez, B. Martel, P. Jefferson, F. Fuchs, V. Muñoz-Sanjosé, F. Bechstedt, C.F. McConville, Valence-band electronic structure of CdO, ZnO, and MgO from x-ray photoemission spectroscopy and quasi-particle-corrected density-functional theory calculations, Phys. Rev. B 79 (2009), 205205.
[30] H. Viltres, O.F. Odio, L. Lartundo-Rojas, E. Reguera, Degradation study of arsenic oxides under XPS measurements, Appl. Surf. Sci. 511 (2020), 145606.
[31] J.S. Hammond, S.W. Gaarenstroom, N. Winograd, X-ray photoelectron spectroscopic studies of cadmium- and silver-oxygen surfaces, Anal. Chem. 47 (1975) 2193–2199.